Porous medium coffee ring effect and other factors affecting the first crystallisation time of sodium chloride at the surface of a drying porous medium

F. Hidri,[1] N. Sghaier,[2] H. Eloukabi,[2] M. Prat,[1,a)] and S. Ben Nasrallah[2]
[1]*INPT, UPS, IMFT (Institut de Mécanique des Fluides de Toulouse), Université de Toulouse, Allée Camille Soula, F-31400 Toulouse, France and CNRS, IMFT, F-31400 Toulouse, France*
[2]*Laboratoire d'Etudes des Systèmes Thermiques et Energétiques de Monastir, École nationale d'Ingénieurs de Monastir, 5000 Monastir, Tunisia*

We study the distribution of ions in a drying porous medium up to the formation of first crystals at the surface. The study is based on comparisons between numerical simulations and experiments with packings of glass beads. The experimental configuration, which is representative of many previous drying experiments, is characterized by the formation of an efflorescence fairy ring at the surface of the porous medium. The preferential formation of crystals at the periphery is explained by the combined effect of higher evaporation fluxes at the surface periphery, as in the classical coffee ring problem, and variations in the porosity near the wall bordering the packing. It is shown that both effects have a great impact on the time marking the occurrence of first crystals, which is referred to as the first crystallization time. The experiments indicate that the first crystallization time increases with a decreasing bead size for a given initial ion concentration. This is explained by the variation with bead size of the characteristic size of the near wall region where a preferential desaturation of the sample occurs as a result of the porosity increase near the wall. The study also reveals a significant salt supersaturation effect. This represents a noticeable fact in relation with salt weathering issues.
[http://dx.doi.org/10.1063/1.4834356]

I. INTRODUCTION

Evaporation in porous media in the presence of dissolved salts is a topic of a significant interest in relation with several environmental issues involving salt transport in unsaturated porous media such as salt weathering or soil salinisation. Salt weathering[1] refers to the deterioration of building materials resulting from the crystallization of salt in the pores. Soil salinisation[2] is the degradation of soils due to high levels of salt. Plants and soil organisms can be killed or their productivity severely limited on affected lands. For both problems a good understanding of water and ions transport in unsaturated porous medium is needed. In addition to these well identified problems, the question of the impact of a dissolved species on evaporation is of general interest in the context of drying[3] or the injection of CO_2 in aquifer.[4]

In spite of the importance of the afore-mentioned applications and the advances made in recent years,[5–9] the modeling of drying in the presence of dissolved salt and crystallization is not very advanced and can be actually considered as a widely open problem. This is so notably because the interplay between the various transport phenomena occurring during drying and the development of crystallized salt structures forming as a result of the evaporation process are not yet well understood.

In this context, predicting where and when the first crystals form appears as a necessary first step in the development of the field. This problem, i.e., the analysis and modeling of drying in

a)Author to whom correspondence should be addressed. Electronic mail: mprat@imft.fr

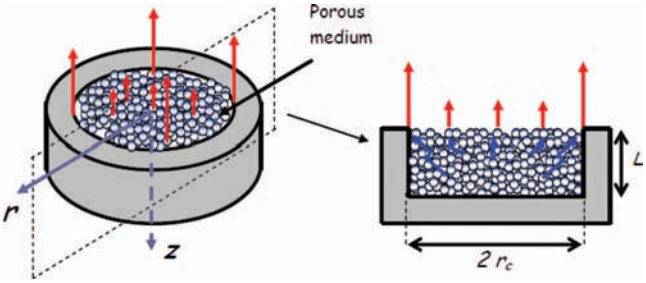

FIG. 1. Sketch of drying experiment with evaporation flux peripheral effect. The greater evaporation flux at the periphery induces greater liquid velocities within the region of the porous medium adjacent to the evaporative surface. These greater velocities induce in turn a greater transport by advection of the dissolved salt in the peripheral region, which leads to the preferential onset of efflorescence at the periphery.

the presence of dissolved ions before and up to occurrence of first crystals has been addressed in previous works.[10–12] The typical situation considered is sketched in Fig. 1.

A porous medium of height L is initially fully saturated with a saline solution and is in contact with dry air at its top surface. All other surfaces are sealed. As explained in several previous works,[10–12] crystallization is expected to occur at the surface of the porous medium when the advection of the ions toward the evaporative surface of the porous medium due to the liquid flow induced in the porous medium by the evaporation process overcomes the ion diffusion transport, which tends to maintain a spatially uniform concentration. In the present work, we are interested in the most classical situations, where the advection effect is sufficient to induce greater ion concentrations at the surface of the porous medium. The first crystals are thus expected to occur at the surface and not inside the porous medium. As in Refs. 10 and 11, we will restrict our attention to the first period of drying, i.e., to the period in which the surface of the porous medium is hydraulically well connected to the liquid contained in the pore space. This is the period in which evaporation takes place at the surface of the porous medium and not inside the porous medium, see Ref. 13 for more details.

Under these circumstances, the consideration of simplifying assumptions, such as a spatially uniform saturation, an effective diffusion coefficient of the ions independent of saturation, and a constant evaporation rate, allows the time of first crystallization to be determined analytically.[11] The time of first crystallization is defined as the time at which the first crystals are observed at the evaporative surface. It corresponds to the time at which the dissolved ion concentration marking the beginning of crystallization is reached at the surface of the sample. This time is referred to as the first crystallization time in this paper.

However, the comparison between the analytical predictions and the experimental results reported in the present paper leads to a very poor agreement, which clearly indicates that the factors affecting the first crystallization time must be further investigated. This is the objective of the paper.

The paper is organized as follows. The experimental setup is briefly described in Sec. II. Experimental results are presented and discussed in Sec. III. The modeling is presented in Sec. IV. The main features of drying process are described in Sec. V. Section VI gives insights into the structure of the ion concentration field during the drying process. The time of the first crystallization time is discussed in Sec. VII. An additional discussion on several factors playing a role in the studied problem is proposed in Sec. VIII. The important issue of supersaturation is discussed in Sec. IX. We close the paper by offering a conclusion in which we summarize the main findings.

II. EXPERIMENTS

Drying experiments are performed with porous samples consisting of packings of approximately spherical glass beads initially saturated with a NaCl aqueous solution contained in a cylindrical vessel (radius $r_c = 1$ cm; depth $L = 1$ cm). Six ranges of bead diameters were used: [5–50 μm], [50–62 μm], [100–160 μm], [200–250 μm], [250–270 μm], and 300 μm.

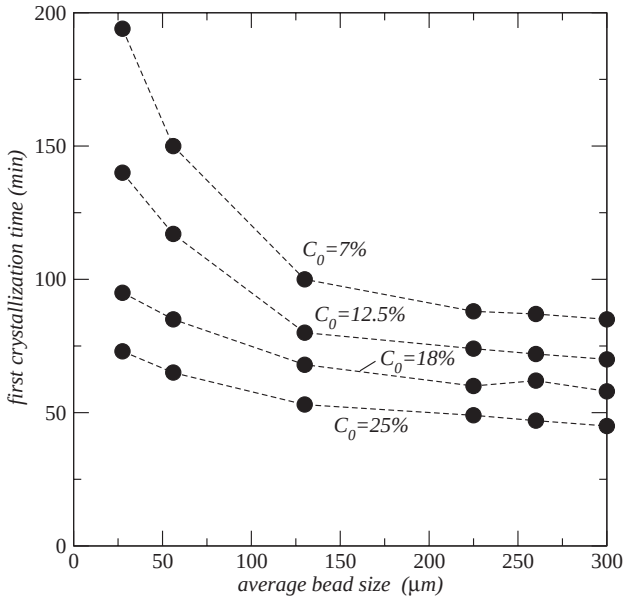

FIG. 2. First crystallization time as a function of average bead size for various initial ion mass fractions (each filled circle corresponds to an experiment). The average bead size is defined as the median size of bead size distribution (see Sec. V)

The sample is set in a chamber of controlled relative humidity (relative humidity $RH_\infty \approx (3 \pm 2)\%$) and temperature ($T \approx 30\,^\circ$C). A Nikon D100 camera with a resolution of 3008×2000 pixels is set above the sample. Images of the sample top evaporative surface are recorded with a frequency of 1 image every 5 min using the acquisition software Nikon Capture Control (version 3). The experiments are performed for four different initial ion mass fractions, namely 7%, 12.5%, 18%, and 25%. Note that the saturation mass fraction C_{sat} is 26.4% for NaCl. The saturation mass fraction corresponds to the solubility of NaCl, i.e., the ion mass fraction in a solution in thermodynamic equilibrium with crystals. The interested reader can refer to Ref. 7 for additional details on the experiments.

The efflorescence onset time, i.e., the first crystallization time, is estimated from the inspection of the images of the porous medium surface taken every 5 min. The crystal should be therefore greater than about one pixel to be detected and there is an uncertainty of at most 5 min since the first crystal can appear between two images.

III. EXPERIMENTAL RESULTS AND FIRST HINTS

The experimental times of first crystallization detected as indicated in Sec. II are shown in Fig. 2. As expected the time of first crystallization increases with a decreasing initial salt fraction. The surprising result is that the time of first crystallization depends on bead size. For a given initial salt mass fraction, it increases with a decreasing bead size. The effect is particularly significant for the smaller beads. This is in contrast to the numerical simulations reported in Ref. 12 and the theoretical analysis presented in Ref. 11, both of which predict that the time of first crystallization is independent of bead size (as long as crystallization occurs during the first drying period, which is the case in our experiments).

The second striking feature of the experimental results is shown in Fig. 3. The crystallization process is characterized by the formation of a crystal fairy ring: the crystals first form at the periphery of the sample. This effect is reminiscent of the well known coffee ring effect.[14] For this reason, we call it the porous medium coffee ring effect. The crystallization is supposed to occur when the ion mass fraction at the surface reaches a sufficiently high value. Let us denote this crystallization mass fraction by C_c. For many salts, there is a supersaturation effect and therefore $C_c > C_{sat}$. This point is, however, somewhat controversial for NaCl.[15,16] It is often admitted that the supersaturation, defined

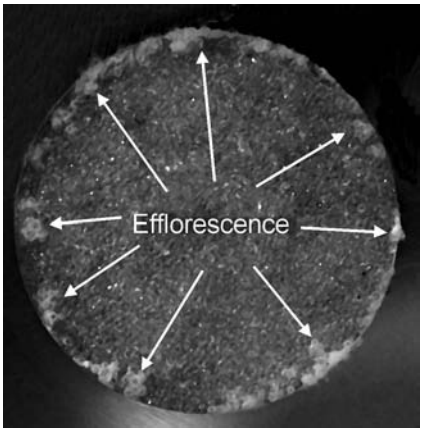

FIG. 3. Efflorescence fairy ring. Top view of surface of porous medium for the beads 300 μm in diameter shortly after the beginning of crystallisation. The efflorescence is clearly visible all along the periphery of the surface of porous medium.

in this paper as $\sigma = C_c/C_{sat}$, is close to 1 for NaCl. However, a supersaturation as high as 3 has been obtained experimentally under particular circumstances[17] whereas experiments in capillary tubes lead to supersaturation of the order of 1.7.[46] Thus, it is reasonable to assume that a supersaturation effect can be present in our experiment. As we shall see, one of the major conclusion of the present work is indeed the existence of a significant supersaturation effect, at least in our experiments. This controversial but very important issue is further discussed at the end of the paper.

Regardless of the exact level of supersaturation, Fig. 3 indicates that the crystallization mass fraction C_c is first reached at the periphery of the sample surface. This is in contrast to the assumptions made in the numerical/theoretical works presented in Refs. 11 and 12, where the problem was considered as one dimensional. By contrast, the preferential formation of first crystals at the periphery clearly indicates a two-dimensional effect.

The results reported in Ref. 8 suggest that the evaporation flux is in fact non uniform at the surface of the porous medium and greater at the periphery for the configuration of the experiments. This is sketched in Fig. 1. As it will make clear later in the paper, the greater evaporation flux at the periphery induces a locally greater ion transport by advection in the peripheral region of the porous medium The greater peripheral evaporation flux is thus consistent with the observation that the crystallisation first occurs at the periphery of the porous medium surface. As in the classical coffee ring problem, the results reported in Ref. 8 thus suggest that a greater evaporation at the periphery could explain the ring effect depicted in Fig. 3.

The distribution of the evaporation flux at the surface is difficult to measure experimentally. To approximately estimate the distribution, one can assume that the flux distribution is similar to the one obtained in the classical coffee ring problem in the limit of very small contact angle (= evaporation from a disk). This distribution can be expressed as[18]

$$j(r) \approx j_0 \left[1 - (r/r_c)^2\right]^{-1/2}, \tag{1}$$

where r_c is the radius of the cylinder, r is the radial distance from the middle of the porous surface, and j_0 is a prefactor, which is such that the integral of (1) over the surface should give the measured evaporation rate J. This gives $j_0 = \frac{\bar{j}}{2}$, where $\bar{j}$ is the average evaporation flux at the surface, $\bar{j} = J/A$ where A is the surface area of the top surface of the porous medium. The distribution is illustrated in Fig. 4. Note the divergence of the flux at the surface periphery. The applicability of Eq. (1) to porous media drying is discussed in Ref. 19 where it is shown that the exact distribution of the flux depends on geometrical details, such as the thickness of the cylindrical vessel containing the beads or related to the shape of the enclosure. Also, as discussed in Ref. 20, free convection effects can slightly modify the distribution compared to the pure diffusion result corresponding to Eq. (1). However this will not change the key point illustrated in Fig. 4: the evaporation flux is greater at the periphery and Eq. (1) represents a reasonable estimate of the evaporation flux distribution.

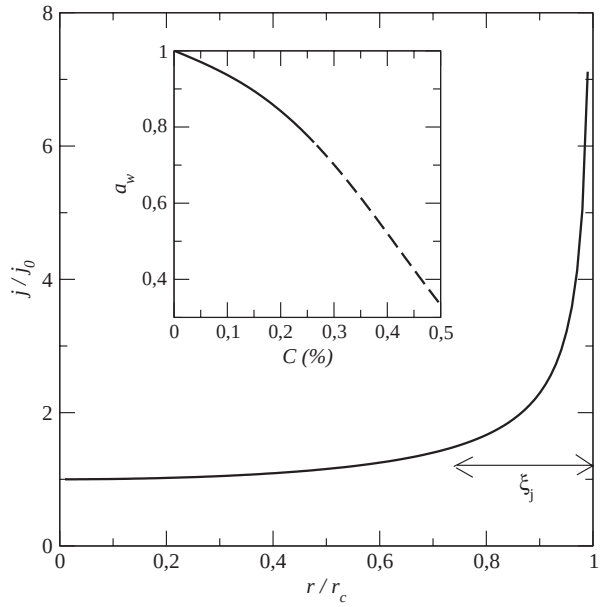

FIG. 4. Expected distribution of evaporation flux at the surface of the porous medium at the beginning of drying process. The evaporation flux is not uniform at the surface of porous medium and much greater at the surface periphery. The inset shows the variation of water activity $a_w = P_{ve}(C)/P_{ve}(0)$ as a function of dissolved salt mass fraction. The dashed line in the inset corresponds to the tentative extension of the curve in the region of ion mass fractions greater than C_{sat} corresponding to supersaturations greater than one.

Although the greater peripheral evaporation flux provides a nice phenomenological explanation to the crystallization ring effect, the situation is however subtler. From the results reported in Ref. 9, we also known that spatial heterogeneities in the porosity and/or the permeability of the medium can have a quite significant effect on the distribution of ions during the evaporation process. As explained in Ref. 9, a local higher porosity means a local lower interstitial velocity (for a given evaporation flux) and thus a locally lower advection of the ions. One other possible effect that can affect the crystallization time is thus the higher porosity expected near the wall in a random packing of spheres.[21] According to Ref. 21, the porosity variation near the solid wall (porosity wall effect) can be expressed as

$$\varepsilon(r_c - r) = \varepsilon_0 \left(1 + \alpha \exp\left(\beta \frac{(r_c - r)}{d}\right)\right), \tag{2}$$

where ε_0, α, and β are the porosity far from the wall ($\varepsilon_0 \approx 0.37$ in a random packing of monodisperse beads) and two numerical factors. The values given in Ref. 21 are $\alpha = 0.98$ and $\beta = -2$, respectively.

Plots of Eq. (2) for $\beta = -2$ and two values of α, namely $\alpha = 0.98$ and $\alpha = 0.1$, are shown in Fig. 5. As can be seen, the variation is typically significant over a distance ξ_ε of about two bead diameters. This size can be compared to the size ξ_j of the peripheral region where the evaporation flux is greater. To estimate the size ξ_j one can consider that the corresponding region is where the flux is greater than the average evaporation flux $\bar{j} = 2\, j_0$. This gives from Eq. (1), $\xi_j/r_c = 0.14$, which gives $\xi_j \approx 1.4$ mm for $r_c = 10$ mm. As a result, ξ_j and ξ_ε are about of the same order of magnitude for the larger beads considered in our experiments but $\xi_j > \xi_\varepsilon$ for smaller beads. Thus there is an interesting variation of the ratio $\xi_j/\xi_\varepsilon \approx 0.14\, r_c/(2d)$ with bead size. This ratio is plotted as a function of bead size in the inset of Fig. 5 showing a variation over a decade.

The objective is now clear. It is to explore the impact of the radial variation of evaporation flux, porosity wall effect and supersaturation effects on the time of first crystallization so as to explain the experimental results reported in Fig. 2.

Before closing this section, it is important to notice that experimental configurations similar to the ones depicted in Fig. 1 are extremely classical in laboratory drying experiments. Thus the

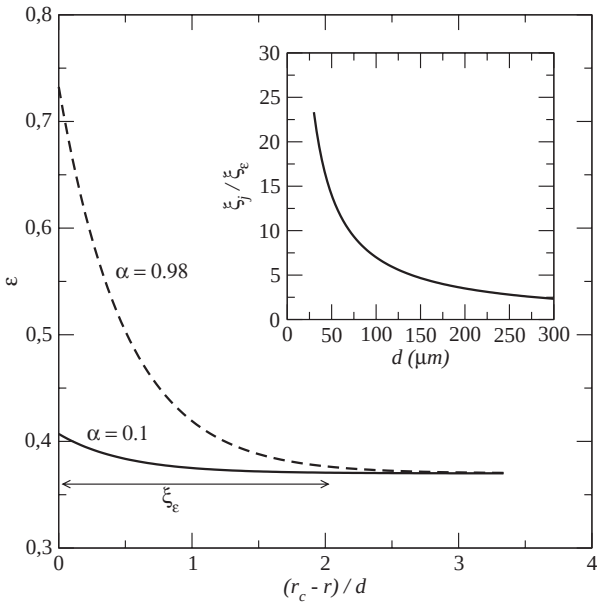

FIG. 5. Porosity wall effect for two values of parameter α computed using Eq. (2). The inset shows the variation of the ratio ξ_j/ξ_ε as a function of average bead diameter.

greater peripheral evaporation flux and the porosity wall effects (when random packings of particles are considered) should be regarded as generic properties of this type of classical experimental configuration.

The study is based on the model of drying and ion transport presented in Sec. IV.

IV. MODELING

A. Continuum model

The first crystallization time is expected to be the time when $C = C_c$ somewhere at the surface of the porous medium. Thus we have to determine the spatio-temporal variations of dissolved salt mass fraction C within and at the surface of the porous sample in order to predict the first crystallization time. The dissolved salt mass transport within the sample is governed by the following equations:

$$\frac{\partial \rho_\ell \varepsilon SC}{\partial t} + \nabla.(\rho_\ell \varepsilon \quad \mathbf{U} \quad SC) = \nabla.\left(\rho_\ell S\varepsilon \quad D_s^* \nabla C\right), \tag{3}$$

$$(\rho_\ell \varepsilon \mathbf{U} SC - \rho_\ell S\varepsilon D_s^* \nabla C).\mathbf{n} = 0, \tag{4}$$

where ε is the porosity of the porous medium, S is the liquid saturation, ρ_ℓ is the liquid density, $\mathbf{U}$ is the average interstitial velocity of the solution (i.e., the average velocity of the liquid in the pores, $\mathbf{U} = \mathbf{U}_D/\varepsilon/\mathrm{S}$ where $\mathbf{U}_D$ is the Darcy's velocity), and D_s^* is the effective diffusive coefficient of the ions, which varies as a function of S. The zero flux boundary condition (4), which applies to each limiting surface of the porous domain and where $\mathbf{n}$ is the unit vector normal to the considered surface, expresses that the dissolved salt cannot leave the porous medium before the onset of crystallization. The initial ion concentration is denoted by C_0 and is spatially uniform.

To solve the above equations, one needs to know at each time step the saturation and velocity fields within the porous domain. These can be obtained from a classical Darcy model describing the flow in the liquid phase. This leads to the following classical governing equations in the unsaturated

region of the sample,

$$\frac{\partial \rho_\ell \varepsilon S}{\partial t} + \nabla.(\rho_\ell \, \mathbf{U}_D) = 0, \tag{5}$$

$$\mathbf{U_D} = -\frac{k k_r}{\mu}(\nabla P_\ell - \rho_\ell \mathbf{g}), \tag{6}$$

where k is the porous medium permeability, μ is the dynamic viscosity of the liquid, $\mathbf{U}_\mathrm{D}$ is the filtration (Darcy) velocity, k_r is the liquid relative permeability and P_ℓ is the pressure in the liquid phase, which is related to the capillary pressure P_c, which is a known function of saturation, by

$$P_\ell = P_{atm} - P_c, \tag{7}$$

where P_{atm} is the pressure in the gas phase, which is assumed uniform and constant (= the atmospheric pressure). Combining Eqs. (5)–(7) leads to the following equation:

$$\varepsilon \rho_\ell C_w \frac{\partial P_\ell}{\partial t} + \varepsilon S \frac{\partial \rho_\ell}{\partial t} = \nabla.\left(\rho_\ell \frac{k k_r}{\mu}(\nabla P_\ell - \rho_\ell \mathbf{g})\right), \tag{8}$$

where $C_w = \frac{dS}{dP_\ell} = -\frac{dS}{dP_c}$.

Here we decided to work with the liquid pressure as primary variable and not the saturation for two reasons: (i) a saturated region can coexist with the unsaturated region in the sample (see below) and (ii) because of the spatial variation in porosity (porosity wall effect) which is much easier to handle with the pressure as primary variable (the pressure is continuous between two unsaturated layers of different porosity while the saturation is not).

Since the sample is fully saturated at $t = 0$, a saturated region can coexist with the unsaturated region located in the upper region of sample because of gravity effect. Assuming that liquid water is slightly compressible (this assumption is in fact a numerical trick for using the same form of equation in the saturated region and the saturated region), the equation governing the liquid pressure in the saturated region reads

$$\varepsilon \rho_\ell \beta \frac{\partial P_\ell}{\partial t} + \varepsilon \frac{\partial \rho_\ell}{\partial C}\frac{\partial C}{\partial t} = \nabla.\left(\rho_\ell \frac{k}{\mu}(\nabla P_\ell - \rho_\ell \mathbf{g})\right), \tag{9}$$

where β is the compressibility coefficient $\beta = \frac{1}{\rho_\ell}\frac{d\rho_\ell}{dP_\ell}$. A classical way[22] of determining the liquid pressure in both the unsaturated and the saturated regions is to combine Eqs. (8) and (9). This yields

$$\varepsilon \rho_\ell (C_w + \beta)\frac{\partial P_\ell}{\partial t} + \varepsilon S \frac{d\rho_\ell}{dC}\frac{\partial C}{\partial t} = \nabla.\left(\rho_\ell \frac{k k_r}{\mu}(\nabla P_\ell - \rho_\ell g_z)\right), \tag{10}$$

with $C_w = 0$, $k_r = 1$, $S = 1$, when $P_\ell > 0$ (taking for convenience $P_{atm} = 0$).

At the impervious limiting surfaces $\partial\Omega_{imp}$, the boundary condition reads

$$\mathbf{U}_\mathrm{D}.\mathbf{n} = 0, \text{ which is expressed as } (\nabla P_\ell - \rho_\ell \mathbf{g}).\mathbf{n} = 0, \tag{11}$$

whereas the continuity of mass flux at the top evaporative surface $\partial\Omega_e$ can be expressed as

$$\rho_\ell \mathbf{U}_\mathrm{D}.\mathbf{n} = -j, \text{ leading to } \rho_\ell \frac{k k_r}{\mu}(\nabla P_\ell - \rho_\ell \mathbf{g}).\mathbf{n} = j, \tag{12}$$

where j, which is counted positively, is the evaporation flux at the surface (note that $\mathbf{n}$ should therefore be considered as the inward normal unit vector).

The initial condition is $S = 1$ everywhere in the porous domain at $t = 0$, that is $P_\ell = 0$. Neglecting the variation of liquid density with salt concentration, it is better to express the above problem using as main variable $H = P_\ell - \rho_\ell g z$ for a better numerical efficiency. This yields

$$\varepsilon \rho_\ell (C_w + \beta)\frac{\partial H}{\partial t} = \nabla.\left(\rho_\ell \frac{k k_r}{\mu}\nabla H\right), \tag{13}$$

with $\rho_\ell \frac{k k_r}{\mu}\nabla H.\mathbf{n} = j$ at $\partial\Omega_e$, $\rho_\ell \frac{k k_r}{\mu}\nabla H.\mathbf{n} = 0$ at $\partial\Omega_{imp}$, and $H = -\rho_\ell g z$ at $t = 0$.

Once the field H is determined, the saturation field S is determined from the relationship between P_c and S with $P_c = -H - \rho_\ell g z$; the filtration velocity field is then computed from $\mathbf{U_D} = -\frac{k k_r}{\mu}\nabla H$.

Although we neglect for simplicity in what follows the variation of density and viscosity with salt mass fraction, it should be clear, however, that the ion transport problem (Eqs. (2) and (3)) and the flow problem are fully coupled. The coupling comes from the decrease of water activity a_w with increasing ion mass fraction,[23] as depicted in the inset of Fig. 4. The water activity $a_w = P_{ve}(C)/P_{ve}(0)$is the ratio of equilibrium vapor pressure at the surface of an aqueous solution to the equilibrium vapor pressure at the surface of pure liquid water. The change in the water activity with ion mass fraction affects the evaporation flux j at the surface of the porous medium. The later is expressed as

$$j = h(P_{ve}(C) - P_{v\infty}), \tag{14}$$

where $P_{ve}(C)$ and $P_{v\infty}$ are the equilibrium water vapor pressure and vapor pressure in the surrounding air; h is the mass transfer coefficient at the porous medium surface. In our model, h can vary spatially over the porous medium surface but not in time. As further discussed in Sec. VIII, this is an approximation when the ion mass fraction varies in time and in space at the surface of the porous medium. To take into account the non-uniformity of the evaporation flux at the surface of the porous medium in the simulation, the interfacial mass transfer coefficient is thus defined from Eq. (1) as

$$h(r) = \frac{j_0\left[1-(r/r_c)^2\right]^{-1/2}}{(P_{ve}(0) - P_{v\infty})}, \tag{15}$$

where j_0 is the value corresponding to drying with pure water. To obtain a solution, the parameters, ε, β, k, k_r, P_c, D_s^* and fluid or equilibrium properties $P_{ve}(C)$, ρ_ℓ, and μ should be specified. This is done below in the sub-section devoted to the numerical solution.

B. Analytical solution

The time of first crystallization can be obtained analytically[11] when the following simplifying assumptions are made: the saturation field is spatially uniform at any time, the effective diffusion coefficient D_s^* is constant (does not depend on saturation), the fluid properties are constant (do not depend on C), the evaporation flux j is constant in time and in space (which implies that the effect of ion concentration on water activity is neglected). This solution reads

$$\sigma C_c = C_0\left[1 + \frac{P_e^2\tau}{(1-Pe\tau)^2}\right], \tag{16}$$

where $\tau = tD_s^*/L^2$ is the dimensionless crystallization time and Pe is the Peclet number characterizing the competition between the ion advection and diffusion transports. The Peclet number is expressed as $Pe = \frac{UL}{D_s^*}$, where the interstitial velocity U and the effective diffusion coefficient D_s^* are estimated at the beginning of drying ($t = 0$). The Peclet number appears when Eq. (3) is expressed in dimensionless form using the height of sample L as characteristic length. Expressing Eq. (3) in dimensionless form has been presented several times, e.g., Refs. 10–12 and therefore will not be repeated in the present paper. From (12) and noting that U is the average interstitial velocity and not the Darcy velocity, we obtain $Pe = \frac{\bar{j}L}{\rho_\ell \varepsilon D_s^*}$, where $\bar{j}$ is the average evaporation flux at the surface of the porous medium at $t = 0$. Notice that Eq. (16) is strictly valid only in the limit of sufficiently high Peclet numbers. As noted before, Eq. (16) does not depend on bead size.

C. Numerical solution

The numerical solution allows to relax several quite restrictive assumptions made to obtain Eq. (16). However, the numerical solution requires to specify several parameters, namely the porosity ε, permeability k, relative permeability k_r and the effective diffusion coefficient D_s^*, the retention curve $P_c(S)$. Considering packing of monodisperse spherical beads, k is estimated using the classical Carman-Kozeny relationship $k = \frac{\varepsilon^3 d^2}{180(1-\varepsilon)^2}$ where d is the bead diameter. The relative permeability is expressed as $k_r(S) = \left(\frac{S-S_c}{1-S_c}\right)^3$, see Ref. 24, whereas the effective diffusion coefficient is given by $D_s^* = \varepsilon^{0.4}\left(\frac{S-S_c}{1-S_c}\right)^{1..5} D_s$, e.g., Ref. 25, where D_s is the ion diffusion coefficient in free water

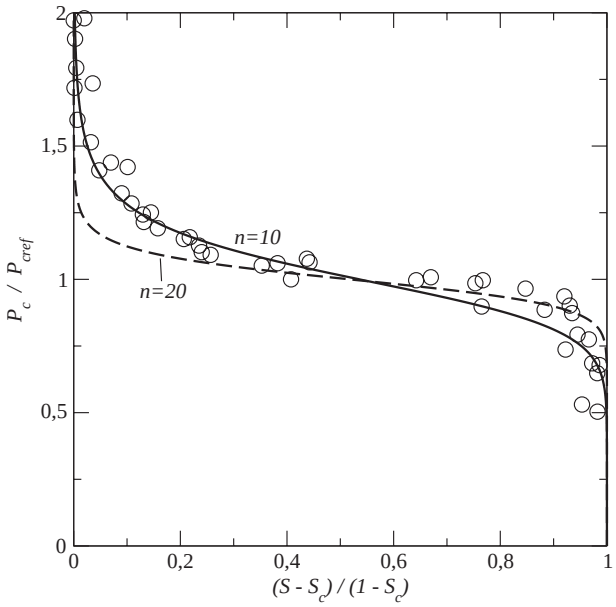

FIG. 6. Reduced retention curve. The solid and dashed lines correspond to the van Genuchten relationship for $n = 10$ and $n = 20$, respectively. The symbols correspond to the experimental measurements presented in Ref. 28 for packing of monodisperse beads.

($D_s = 1.3 \times 10^{-9}$ m^2/s). The retention curve is obtained by fitting the parameters of the classical relationship proposed by van Genuchten,[26]

$$\frac{S - S_c}{1 - S_c} = \frac{1}{\left[1 + \left(\frac{P_c}{P_{cref}}\right)^n\right]^m}, \tag{17}$$

with $m = 1 - \frac{1}{n}$ and $P_{cref} = \frac{6(1-\varepsilon)\gamma}{\varepsilon d}$, where γ is the surface tension ($\gamma = 72 \times 10^{-3}$ N/m for pure water). The parameters n and S_c are determined from experimental data for packing of monodisperse spheres.[27,28] From the data reported in Ref. 27 we take $S_c = 0.1$. Then, we have tried to adjust the van Genuchten correlation on the data from Ref. 28. Examples of fitting are presented in Fig. 6. P_{cref} is classically referred to as the capillary entry pressure. The capillary entry pressure corresponds to the minimum pressure difference between the two fluids allowing the breakthrough of the non-wetting phase through a porous sample. The capillary entry pressure plays a key role in controlling the saturation variation during drying between regions of different porosity in variable porosity media.[29]

As can be seen, it is not easy to have a good fit over the whole range of reduced saturation. On the ground that the beads are not truly monodisperse in our experiments (this should lead to a less flat retention curve in the region of intermediate saturations compared to a strictly monodisperse packing), we have taken $n = 10$ in all the simulations presented in what follows. The compressibility coefficient β for water is $\beta \approx 4 \times 10^{-10}$ Pa^{-1}; $\mu = 10^{-3}$ *Pl*, and $\rho_\ell = 1000$ kg/m^3.

The surface average interfacial mass transfer coefficient is deduced from the experimental data for pure water,[7] $\bar{h} = \bar{j}_{\rm exp}/(P_{ve}(0) - P_{v\infty})$, where $\bar{j}_{\rm exp} = -\frac{1}{A}\left.\frac{dm}{dt}\right|_{t=0}$; A is the area of the porous medium top surface and m is the mass of the sample (measured every 2 min thanks to a scale). From the data reported in Ref. 7, this gives $\bar{j}_{\rm exp} = 10^{-4}$ kg/m^2/s (for pure water), from which we obtain $\bar{h} = \bar{j}_{\rm exp}/(P_{ve}(0) - P_{v\infty}) = 2.43 \times 10^{-8}$ kg/m^2/Pa/s.

The variation of equilibrium vapor pressure with ion mass fraction $P_{ve}(C)$ is obtained by fitting a polynomial expression to the data reported in Ref. 23. One problem is that we need values of $P_{ve}(C)$ in the range $[C_{sat}, C_c]$, i.e., above C_{sat}, because of the supersaturation effect. We have simply used the polynomial expression fitted on the available experimental values in the range $[0, C_{sat}]$ also in the range $[C_{sat}, C_c]$. This gives the variation of water activity reported in the insert in Fig. 4. As

the result, the water activity can drop below 0.75 because of the supersaturation effect. Note that the variations of μ and ρ_ℓ with ion mass fraction C have been neglected in the present effort in order to simplify a bit the numerical procedure.

A problem is to incorporate the porosity variation given by Eq. (2) into the continuum approach underlying the modelling presented in this section since the porosity variation given by Eq. (2) takes place over a distance of only two bead diameters, thus *a priori* smaller than the size of the so-called representative elementary volume (REV).[22] The direct use of Eq. (2) leads to a rapid and very strong desaturation of a very thin layer (its thickness is much less than a fraction of bead diameter!) along the wall of the cylinder containing the porous medium, which does not appear consistent with the continuum picture. Although the problem would certainly deserve a specific study, we have adopted the simpler approach consisting in smoothing the wall porosity variation. Our simple method is still to use Eq. (2) but with a value for the numerical factor α much smaller than the one given in Ref. 21. We took $\alpha = 0.1$. The corresponding variation of porosity is shown in Fig. 5. As we shall see the wall porosity effect, albeit smoother than considered in Ref. 21, is quite significant. Note that the same bulk porosity $\varepsilon_0 \approx 0.37$ is used for all packings in the simulations.

Since the beads used in the experiments are not strictly monodisperse (except for the size 300 μm), we also have to specify an equivalent bead diameter to run the simulations. In the absence of detailed information on the bead size distribution we simply used the median size, i.e., $d = 27.5$ μm, 56 μm, 130 μm, 225 μm, and 300 μm for the ranges [5–50 μm], [50–62 μm], [100–160 μm], [200–250 μm], [250–270 μm], and 300 μm, respectively.

When all the parameters have been specified, the system formed by Eqs. (3) and (13) and associated boundary conditions and initial conditions is solved numerically using the commercial simulation software COMSOL Multiphysics. The validity of the numerical procedure has first been tested by obtaining a good agreement between the theoretical predictions given by Eq. (16) with the 1D numerical predictions for a sufficiently high Peclet number using a constant diffusion coefficient, a constant activity for large beads and g = 0 (using large beads with g = 0 ensure that the saturation is spatially uniform as shown in Sec. V). The two-dimensional simulations are run using cylindrical coordinates. One obvious concern is the impact of the mesh on the results, especially because the evaporation flux diverges at $r = r_c$ according to Eq. (1). First it should be noted that the evaporation rate, i.e., the integration of Eq. (1) over an elementary surface does not diverge. We classically ran the simulations for different meshes, using a much refiner mesh along the wall and the evaporative surface with the finest elements located in the region of the corner formed by the evaporative surface and the vessel wall. It was found that using elements of size of about 1 μm in the corner region, elements of size 10 μm elsewhere along the wall and the evaporative surface (the size of the elements then increases inside the computational domain away from these two surfaces) led to results independent of mesh.

V. MAIN FEATURES OF DRYING PROCESS

As noted before, since Eqs. (3) and (4) governing the ions transport explicitly depend on the saturation field, it is important to understand the distribution of S during the drying process. The main features of this distribution are not greatly affected by the presence of the salt. Thus, it is sufficient to discuss the situation for pure water.

The factors affecting the saturation distribution during a drying process such as the one considered here are well known.[30] Gravity and viscous effects tends to induce saturation gradient whereas dominant capillary effects lead to spatially uniform saturation. Consider first the possible influence of viscous effects. Neglecting gravity effects, we deduce from Eq. (12), the following estimate $\frac{\Delta P_\ell}{L} = O\left(\frac{\mu j}{\rho_\ell k k_r}\right)$, where ΔP_ℓ represents the pressure variation in the liquid due to viscous effects. Then we form the ratio $\Delta P_\ell/(0.3P_{\text{cref}})$, which allows us to determine when the viscous effects are significant compared to the capillary effects: $Ca = \frac{\Delta P}{0.3P_{cref}} = \frac{\mu j \varepsilon d L}{1.8\rho_\ell k k_r (1-\varepsilon)\gamma}$. The factor 0.3 comes from the observation that the saturation variation is significant in Fig. 6 for a variation of reduced capillary pressure of about 30%. This ratio can be interpreted as a capillary number. Similarly we can form a Bond number, $B = \frac{\rho_\ell g L}{0.3P_{cref}}$, which compares gravity effects to capillary effects. The criterion

is that the viscous effects (the gravity effects respectively) are negligible when Ca (B respectively) is lower than 0.01. The computation of Ca indicates that viscous effects are negligible for all the bead sizes considered in the experiments provided that the saturation remains greater than about 0.3 (the minimum saturation reaches in our simulations is 0.457) for the beads 27.5 μm in diameter (which is the most critical size as regards the possible influence of viscous effects) whereas the computation of B indicates that gravity effects are not negligible except for the smallest beads. This is further discussed in what follows.

In other terms, the distribution of S during drying is essentially quasi-static. This distribution can therefore readily be deduced from the equation,

$$\frac{dP_\ell}{dz} = \rho_\ell g, \tag{18}$$

which gives

$$P_\ell = P_\ell(0) + \rho_\ell g z, \tag{19}$$

which is combined with the retention curve Eq. (17) to give

$$\frac{S - S_c}{1 - S_c} = \frac{1}{\left[1 + \left(\frac{-P_\ell(0) - \rho_\ell g z}{P_{cref}}\right)^n\right]^m} \text{ if } P_\ell(0) + \rho_\ell g z \leq 0 \text{ and S} = 1 \text{ if } P_\ell(0) + \rho_\ell g z > 0. \tag{20}$$

Notice that Eq. (20) can readily be used in the presence of spatial variation in porosity through the dependence of P_{cref} with porosity. Since the capillary entry pressure P_{cref} decreases near the wall because of the porosity wall effect ($P_{cref} = \frac{6(1-\varepsilon)\gamma}{\varepsilon d}$, thus decreases when ε increases), the saturation should decrease near the wall so as to maintain along each horizontal line the same liquid pressure corresponding to the hydrostatic equilibrium, see also Ref. 29 for further details. The result is therefore a preferential desaturation of the near wall region where the porosity varies. This is illustrated in Fig. 7. This is further illustrated in Fig. 8 which shows a typical saturation variation near the wall resulting from the porosity wall effect.

As mentioned before, the effect is a marked preferential desaturation of the wall region. The typical size of the dryer zone near the wall is ξ_ε, which is equal to about 2 bead diameters. Thus, the smaller the beads, the narrower the size of the wall region where the saturation is less than in the bulk. The inset in Fig. 8 illustrates the impact of gravity effects on the saturation distribution, which is noticeable for the larger beads used in our experiments but negligible for the smaller beads. Naturally, we have checked that the numerical solutions obtained by Eq. (13) led to the same saturation fields as the ones given analytically by Eq. (20).

In summary, the saturation distribution during the drying process is essentially a quasi-static distribution resulting from the equilibrium between capillary and gravity effects. The gravity effects are however negligible for the smaller beads, which lead in this case to a quasi-uniform saturation along the depth of sample. The porosity wall effect has a significant effect on the radial distribution of the saturation. It induces the formation of a thin region of size of about two bead diameters near the wall where the saturation is significantly lower than away from the wall. It is worth realizing that the preferential desaturation near the wall has nothing to do with the greater evaporation flux near the wall since viscous effects have a negligible influence on the phase distribution in our experiments. The near wall desaturation is due to the increase in porosity near the wall since the continuity of capillary pressure implies a lower saturation where the porosity increases. Although very close to hydrostatic, the saturation distribution is of course not exactly hydrostatic since the evaporation at the porous surface induces a liquid flow and thus a velocity field in the liquid phase within the porous medium. This velocity field is computed from the numerical solution. An example of computed interstitial velocity fields showing the greater velocities in the peripheral region near the surface is depicted in Fig. 9.

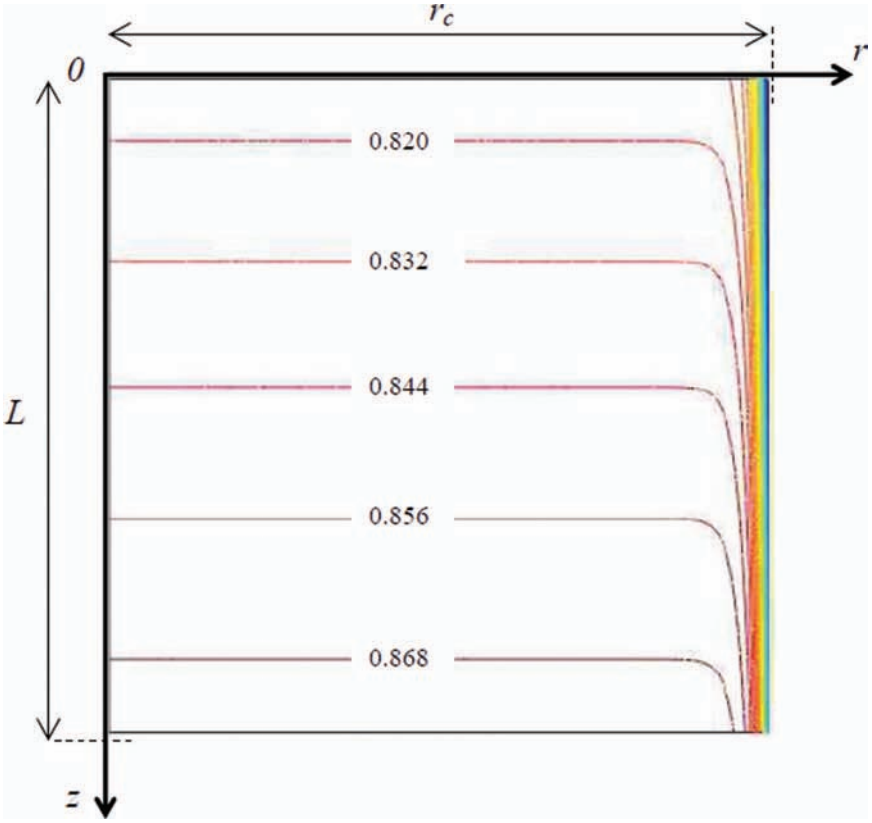

FIG. 7. Saturation isocontours at the onset of crystallization for the case $C_0 = 7\%$, $\sigma = 2$, $d = 300$ μm). The variation in saturation along the vertical is due to the gravity effects whereas the saturation gradients near the wall are due to the porosity wall effect (see text). The saturation in the near wall region varies between 0.515 (minimum value at upper right corner) and 0.8. The size of the high saturation gradient region near the wall varies as ξ_ε, thus decreases by about one order of magnitude when the bead size decreases from 300 μm to 30 μm.

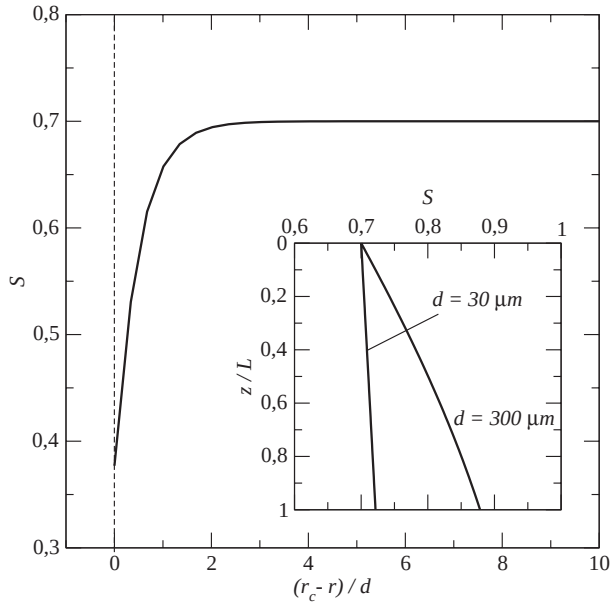

FIG. 8. Example of saturation profile near the wall at $z = 0$ (porous medium surface) when the saturation is 0.7 far from the wall ($d = 300$ μm). The inset shows the saturation profile as a function of z far from the wall for two bead sizes when the saturation is 0.7 at the surface. Note the influence of gravity effects on the profile for the larger beads.

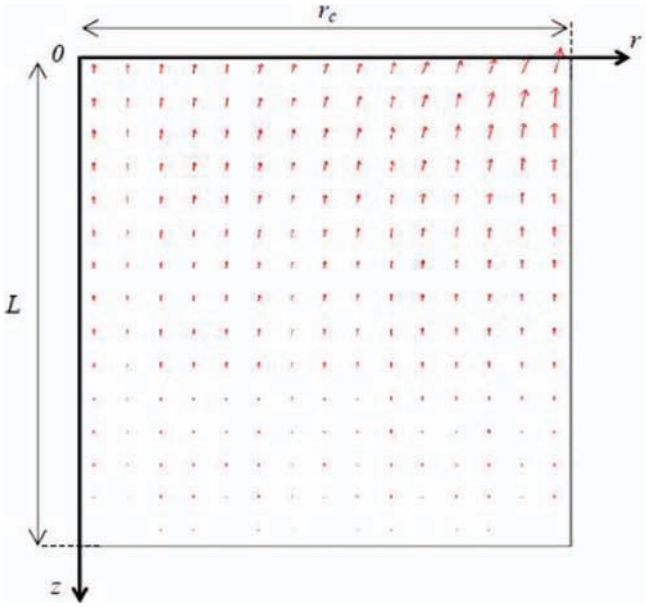

FIG. 9. Example of interstitial velocity distributions (at $t =$ first crystallization time, $d = 300\ \mu$m, $\sigma = 2$, $C_0 = 7\%$) showing greater interstitial velocities in the peripheral corner region.

VI. STRUCTURE OF ION CONCENTRATION FIELD

The main features of salt mass fraction field during drying are summarized in Figs. 10 and 11. The variation of ion mass fraction with depth is characterized by the formation of ion mass fraction gradient zone adjacent to the evaporative surface. Below this zone of size denoted by ζ(t), the ion

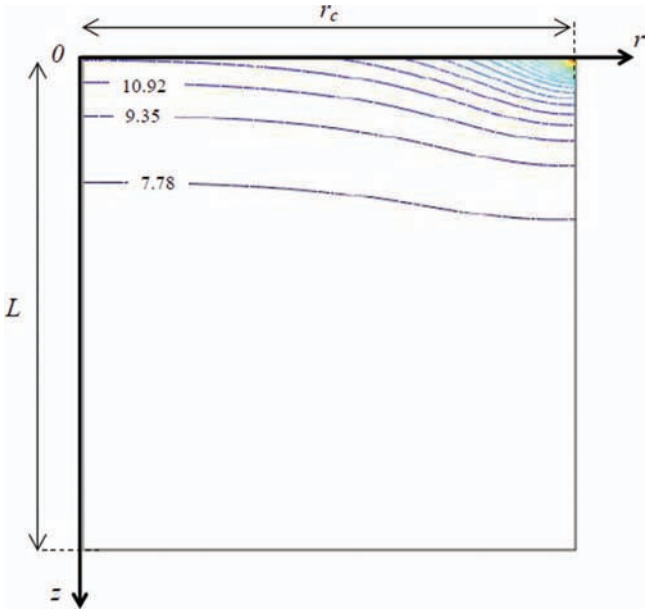

FIG. 10. Ion mass fraction isocontours at the onset of crystallization for the case $C_0 = 7\%$ and the beads 300 μm in diameter ($\sigma = 2$). Because of higher evaporation fluxes at the porous medium surface periphery (see Fig. 5), the highest ion mass fractions localize at the periphery of the surface of porous medium. As explained in the text, the porosity wall effect also contributes to the occurrence of greater ion mass fractions at the surface periphery. The ion mass fraction varies between 7.77% and 52.8%, which is the crystallization mass fraction reached at the upper right corner.

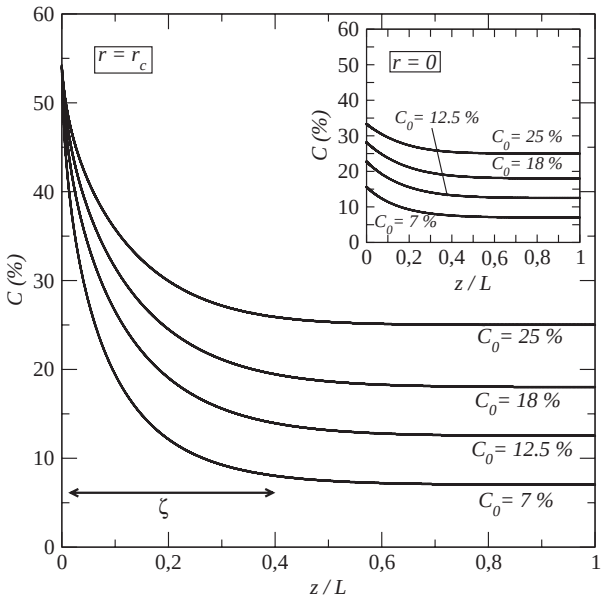

FIG. 11. Examples of ion mass fraction profiles at $r = r_c$ (surface periphery) at the onset of crystallization for various initial ion mass fraction ($d = 27.5$ μm, $\sigma = 2$, porosity wall effect taking into account, external mass transfer coefficient given by Eq. (12)). The ion mass fraction gradient is important only in the region of size ζ near the surface of the porous medium. The inset shows the profiles at $r = 0$ at the same times, thus in the bulk outside of the wall/peripheral region.

mass fraction is spatially uniform. In the gradient zone, the mass fraction increases and reaches a maximum at the evaporative surface. From previous works,[10–12] this the expected profile when the Peclet number $Pe = \frac{\bar{j}L}{\rho_\ell \varepsilon D_s^*}$ is on the order of 1 or greater. In our experiments,[7] $\bar{j} \approx 10^{-4}$ kg/m^2/s, which leads to $Pe \approx 3$. Because of the porosity wall effect and the greater peripheral evaporation flux at the periphery, a greater ion mass fraction is expected at the surface periphery. This is illustrated in Figs. 10 and 11.

More insights can be gained from the consideration of the local effective Peclet number obtained in forming the ratio of advection term and diffusion term in Eq. (3) using $U \approx \frac{\bar{j}}{\rho_\ell \varepsilon S}$ as characteristic velocity and L as characteristic length,

$$Pe_{eff}(r) = \frac{j(r)L}{\rho_\ell \varepsilon(r) S(r) \left(\frac{S(r)-S_c)}{1-S_c} \right) D_s}. \tag{21}$$

As can be seen from Eq. (21), the increase in the evaporation flux at the periphery (see Fig. 4) and the decrease in saturation near the wall induces by the porosity wall effect (see Fig. 8) both contribute to increase the local effective Peclet number whereas the greater porosity at the periphery (see Fig. 5) tends to diminish the local Peclet number. As illustrated in Fig. 12, the net effect is the increase in the local effective Peclet number at the periphery of the surface. As illustrated in the inset of Fig. 12 and expected since the length ξ_ε decreases with a decreasing bead size d, the effective Peclet number is less (for a similar saturation far from the wall at the surface) in the wall region for small beads compared to larger beads. Thus, the bead size do have an impact on the ion mass fraction distribution at the surface because: (i) the surface desaturation due to gravity effects is more marked for large beads (see Fig. 8) and (ii) the wall region desaturation due to porosity wall effects is more confined along the wall for small beads than for larger beads. More precisely, the size of the high saturation gradient region near the wall (see Fig. 7) varies as ξ_ε, thus decreases by about one order of magnitude when the bead size decreases from 300 μm to 30 μm ($\xi_\varepsilon \approx 2d$).

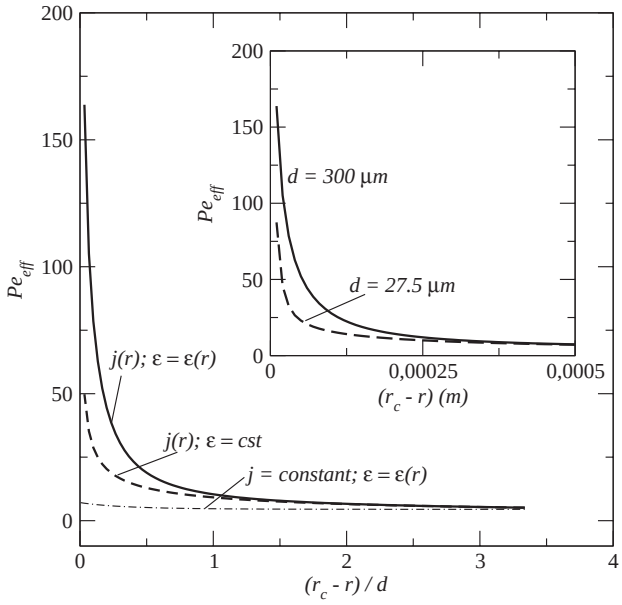

FIG. 12. Local effective Peclet number as a function of distance from porous domain wall ($d = 300\ \mu$m). The combination of greater evaporation fluxes at the surface periphery and porosity wall effects leads to a much greater advection effect in the region of the porous medium adjacent to the surface periphery. The inset shows the variation of local effective Peclet number for two bead sizes.

VII. FIRST CRYSTALLIZATION TIME

A. Results for the largest beads (d = 300 μm)

We begin by comparing the experimental results and the theoretical and numerical results for the beads of 300 μm in diameter.

The results are presented in Fig. 13. We have first estimated the first crystallization time theoretically from Eq. (16), with $\sigma = 1$ (no supersaturation). To make use of Eq. (16), we use the previously estimated value of Peclet number $Pe = \frac{\bar{j} L}{\rho_\ell \varepsilon D_s^*}$ ($Pe \approx 3$), where again the mean evaporation flux $\bar{j}$ and the effective diffusion coefficient are estimated at $t = 0$: $D_s^* = \varepsilon^{0.4} D_s$ ($S = 1$ at $t = 0$), $\bar{j} = \bar{h}\ (P_{ve}(C_0) - P_{v\infty})$. Using Eq. (16) with $\sigma = 1$ gives the results reported in Fig. 13, which clearly indicates that the time of first crystallization can be severely overestimated when using Eq. (16) indiscriminately. As can been seen from Fig. 13, the numerical 1D computation with $\sigma = 1$ leads to times of first crystallization closer to the experimental values (except for the initial concentration $C_0 = 25\%$). This is a clear indication that it is important to take account the variation of D_s^* with the saturation S and the variation of the evaporation flux resulting from the decrease of water activity with increasing salt mass fraction as well as the gravity effects. We recall that all these effects are neglected in the derivation of Eq. (16). Also, we recall that Eq. (16) has been derived under the assumption of a high Peclet number (greater than 100 typically). The estimates provided by Eq. (16) are necessarily less accurate for the moderate Peclet number characterizing our experiment. Nevertheless the agreement between the 1D numerical computations and the experimental data is clearly poor with a much steeper variation of first crystallization time with initial concentration predicted by the numerical model. Not surprisingly, these results clearly confirm that a 1D approach is here not sufficient owing to the peripheral effects associated with the porosity and evaporation flux spatial variations.

As shown in Fig. 13, the full 2D simulations with $\sigma = 1$ leads to a variation of the first crystallization time with initial concentration in much better agreement with the experiments, i.e., much less steep than for the 1D simulations. However, the crystallization times are significantly underestimated. Since recent experiments[17] indicate that the supersaturation can be relatively high

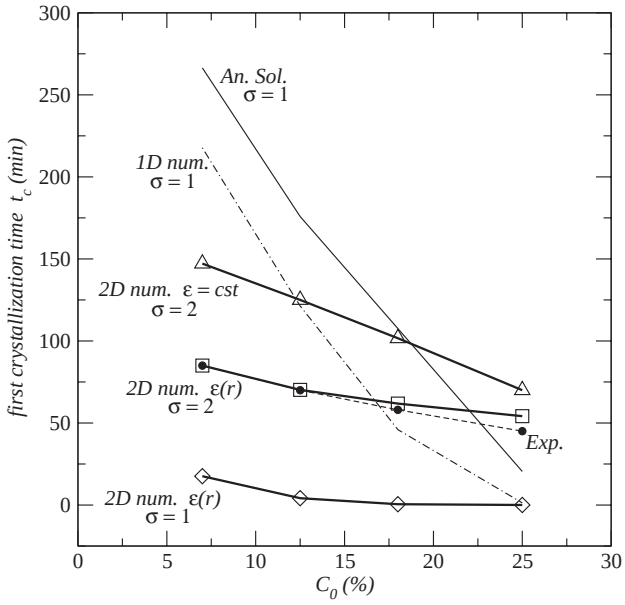

FIG. 13. First crystallization time as a function of initial ion mass fraction. The experimental data (black disks) correspond to the experiments with the beads 300 μm in diameter. The plot labelled "*An. Sol.*" corresponds to the analytical solution given by Eq. (16). The plots labelled "*2D num ε(r)*" and "*2D num ε = cste*" correspond to the 2D numerical simulations with a spatially variable evaporation flux at the surface of porous medium and with the wall effect on the porosity and a uniform porosity respectively. The plot labelled "*1D num*" corresponds to the numerical simulations for a spatially uniform evaporation flux at the surface of porous medium. σ is the supersaturation.

for NaCl, we decided to look at the impact of the supersaturation σ on the results. First, it should be clear from Fig. 13 that increasing the supersaturation can by no means improve the theoretical prediction provided by Eq. (16) nor the results obtained with the 1D simulation since increasing the supersaturation will simply increase the predicted time of first crystallization.

As can be seen from Fig. 13, a quite nice agreement with the experimental data can be obtained with the full 2D model and $\sigma = 2$. Interestingly, the supersaturation 2 estimated from our simulations is greater but comparable to the value 1.7 measured in capillary tubes.[46] As shown in Fig. 13, neglecting the porosity wall effect for the same value of supersaturation leads to overestimate the crystallization time, which was expected from the discussion presented in Secs. VI and VII (the lower saturation near the wall induced by the increase in porosity leads to a greater interstitial velocity and thus lower crystallization times compared to the case where there is no porosity variation). Also the variation with initial mass fraction is steeper than in the experiments when the porosity wall effect is neglected.

B. Results for the various bead sizes

Keeping $\sigma = 2$, the results obtained with the full 2D model for the various bed sizes and initial mass fractions are presented together with the experimental data in Fig. 14. The agreement can be considered as good. In particular, the model captures the increase in the first crystallization time with a decreasing bead size. The effect is due in part to gravity effects which have a greater influence for the larger beads (Fig. 8) but mainly to the change in the length ξ_ε which bead sizes ($\xi_\varepsilon \approx 2d$), which leads to a narrower and narrower region affected by the porosity wall effect when the bead size decreases.

As illustrated in Fig. 15, neglecting the porosity wall effect consistently leads to much smaller variations of first crystallization time with bead size. Also, the predicted crystallization time is greater when the porosity wall effect is not taken into account (the supersaturation is kept equal to 2 for all the simulations presented in this section). However, it can pointed out that the beads

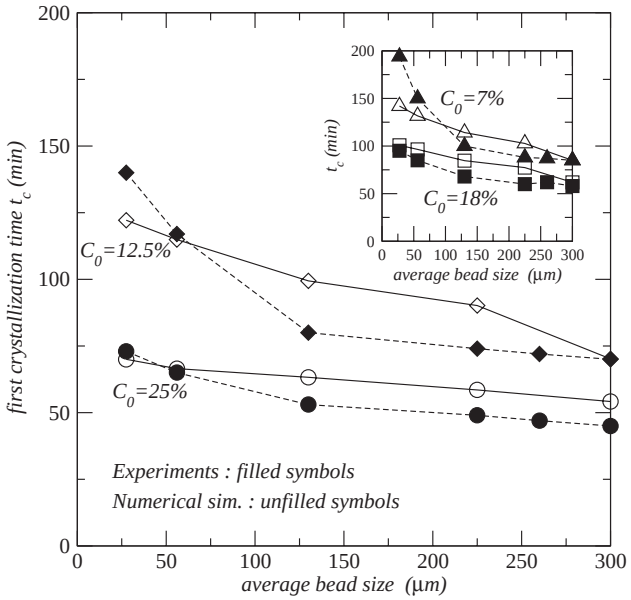

FIG. 14. Comparison between experimental times of first crystallisation and computed values using the full 2D model with supersaturation $\sigma = 2$ for various bead sizes and various initial ion mass fractions.

corresponding to the smallest beads [5–50 μm] are far from monodisperse. Thus it could be argued that the porosity wall effect is much less marked for this particular range of bead sizes than for the narrower distributions of bead size corresponding to the other sizes used in the experiments. Since the predicted time of first crystallization is greater when the porosity wall effect is ignored, it is tempting to assume that the porosity wall effect can be neglected for the packing with the beads in the range [5–50 μm]. Assuming the porosity wall effect negligible for this packing only (the porosity wall effect is thus taken into account for the other packings) lead to the comparison with experimental data depicted in Fig. 16, which is better than the one reported in Fig. 14.

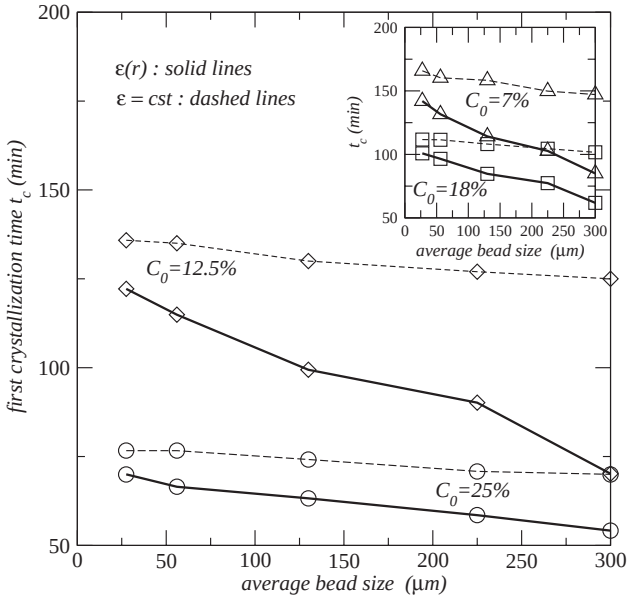

FIG. 15. Comparison between times of first crystallisation computed using the full 2D model and the times computed neglecting the porosity wall effect for various bead sizes and various initial ion mass fractions and supersaturation $\sigma = 2$.

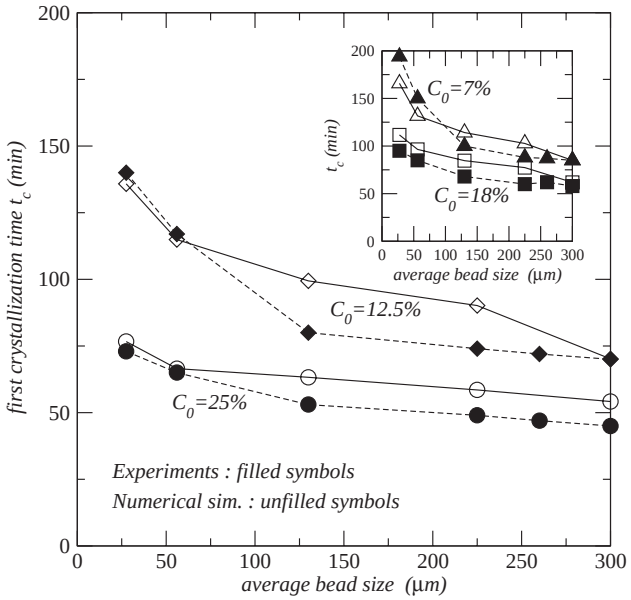

FIG. 16. Comparison between experimental first crystallisation times and computed values using the 2D model with supersaturation $\sigma = 2$ for various bead sizes and various initial ion mass fractions. The computed values for $d = 27.5$ μm were obtained assuming $\varepsilon = cste$ (no porosity wall effect) whereas the values for other bead sizes were obtained assuming $\varepsilon = \varepsilon(r)$, thus taking into account the porosity wall effect.

VIII. DISCUSSION

In this section, we offer a short discussion on various effects that might play a role in the studied problem and could explain in part why a still better agreement with experimental data was not achieved.

We have assumed that the bulk porosity was the same for all the bead packings. As shown in Ref. 9 and also by the impact of the porosity wall effects on our results, the porosity is a sensitive parameter. This can be illustrated simply from Eq. (16). Using Eq. (16) under the same conditions as in Sec. VII and varying only the porosity lead to first crystallization times equal to 226 and 264 min, thus a 17% increase, when the porosity is varied from 0.37 to 0.4 for the case $C_0 = 7\%$. However, the porosity can be expected to be lower for the polydisperse packing [5–50 μm] than for the narrower packings corresponding to the other bead sizes. A lower porosity implies greater interstitial velocities and thus shorter first crystallization times. Thus a lower bulk porosity cannot be invoked to explain the significant increase in the crystallization time observed for this particular packing. Thus a less significant porosity wall effect seems a much better explanation as discussed at the end of Sec. VII. However, owing to its significance in our results, the porosity wall effect would deserve to be characterized more rigorously in the framework of the continuum approach to porous media.

As pointed out in Ref. 9, only the heterogeneities present in the ion mass fraction gradient zone of size ζ adjacent to the evaporative surface (see Fig. 11) play a role. Thus a greater porosity only in the top layer adjacent to the porous medium surface is sufficient to increase the first crystallization time. Therefore, it could be interesting to investigate if there exists a bead size dependent region adjacent to the top surface of packing where the beads arrangement could be slightly different from further away from the surface.

Regarding the modeling of the external mass transfer, we have considered that the mass transfer coefficient can vary in space, Eq. (15) but assumed that it does not vary in time. According to the results presented in Ref. 31, this can be questioned. In fact, our assumption is strictly valid when the vapor pressure at the surface is spatially uniform. However, as illustrated in Figs. 9 and 17, the ion mass fraction over the surface becomes spatially non-uniform as a result of the greater flux at

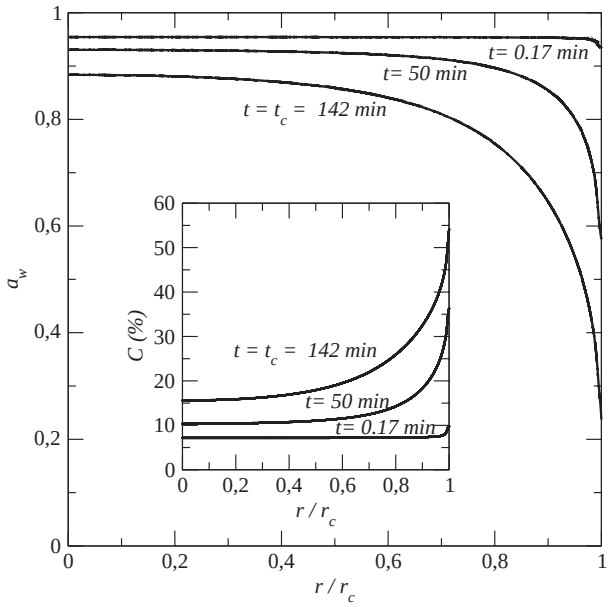

FIG. 17. Computed distribution of water activity at the surface of porous medium at various times (2D simulations with porosity wall effect and a non-uniform evaporation flux distribution, $\sigma = 2$, $d = 27.5\ \mu$m). The inset shows the corresponding ion mass fraction distribution at the surface of porous medium.

the periphery, which in turn induces a non-uniform distribution of the vapor pressure at the surface (this is illustrated in Fig. 17). This change in the boundary condition for the external mass transfer should change the structure of the water vapor partial pressure field in the external air and especially near the surface of the porous medium. As a result, this should modify the distribution of the mass transfer coefficient at the surface. Physically, the lower vapor pressure at the periphery resulting from the greater ion concentration contributes to decrease the peripheral evaporation flux (and this is taken into account in our simulation as illustrated in Fig. 18) but also induces a lateral flux from the central region (where the vapor pressure is greater) toward the peripheral region (this is not taken into account in our simulations). One option to take into account properly the change in the external mass transfer would be to avoid using the concept of external mass transfer coefficient by solving explicitly the equations governing the external mass transfer.[8,31,32] This represents a heavy task since these equations should be solved repeatedly together with Eqs. (3) and (10) governing the ion transport and the evolution of saturation in the porous medium.

Perhaps more significant is the fact that the solution given by Eq. (1) corresponds to water vapor mass transport controlled by diffusion. According to the results presented in Ref. 33 it is likely that free convection effects induced by the spatial variation in density of the water vapor–air gas mixture are non-negligible in our experiments. According to the numerical simulations reported in Ref. 20, the shape of the distribution is modified in the presence of free convection effects. However, this does not change the main feature of this distribution: the increase of the flux with the radial distance r with much greater fluxes at the periphery. In short, the evaporation flux distribution in the experiments is likely to differ to some extent from the distribution given by Eq. (1) but not sufficiently for changing the main conclusions of the present study.

We have assumed that the supersaturation ($\sigma \sim 2$ in our simulations unless otherwise mentioned) was independent of bead size. This is an open question. This is consistent with preliminary experiments in capillary tubes, which do not indicate a variation in supersaturation with a decreasing tube size.[46] A decrease in supersaturation with decreasing bead size is not consistent with the increase in the first crystallization time with decreasing bead size observed in our experiments. Thus, it seems reasonable to conclude that the supersaturation does not vary significantly with bead size in our experiments.

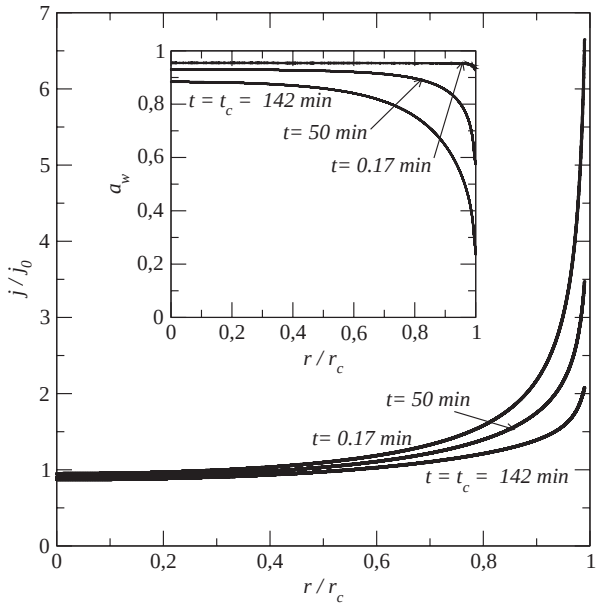

FIG. 18. Computed distribution of evaporation flux at the surface of porous medium at various times (2D simulations with porosity wall effect and a non-uniform evaporation flux distribution, $\sigma = 2$, $d = 27.5\ \mu$m). The inset shows the corresponding activity distribution at the surface of porous medium.

A more "radical" option is to question the relevance of the classical continuum approach to porous media to properly simulate the drying process in the case of our experiments since the evaporation flux variation and porosity variation occur over a few grain sizes. It is well known from pore network studies of drying,[30,34] that the capillary regime is the most difficult to model using classical continuum concepts since this regime is essentially an invasion percolation regime, see Ref. 30 for more details. Thus, it might be necessary to analyze our experiments within the framework of pore network models for a better understanding of the experimental results. However, whereas there exist many studies of drying based on pore network model and the associated framework, see Ref. 34 for numerous references, the pore network modeling of drying in the presence of dissolved ion is still essentially an open project, see Ref. 35 however. Thus, we leave this type of investigation for a future work, noting that coupling such a pore network model with an adequate model of external mass transfer is also a challenge.

To close this section, we will just comment briefly the possible influence of liquid films. As shown in the studies[36–39] related to the pore network modeling of drying, liquid films can have a strong influence on the duration of the various phases of drying. As discussed in Ref. 40, the films can also transport the ions up to the surface of the porous medium. However, the spatial extent of the films, that is the distance over which the ions can be transported by the films, is scale dependent. Because of viscous effects within the films, the maximum extent of the films in the system decreases with decreasing bead size. In short, the films could carry the ions up to the surface for sufficiently large beads whereas this possibility of transport would become increasingly negligible for smaller and smaller bead sizes. This film effect, which of course needs to be assessed quantitatively, could thus also contribute to the increase in the time of first crystallization with decreasing bead size observed in the experiments.

IX. SODIUM CHLORIDE CRYSTALLISATION AND SUPERSATURATION

The value 2 of supersaturation obtained from the comparison between the simulations and the experiments is not claimed as being the exact value in the experiment since there are uncertainties in the modeling, notably as regards the exact distribution of the evaporation flux at the surface and the

correct modeling of the porosity wall effects within the continuum approach framework. For example, the consideration of a slightly different evaporation flux distribution, due to free convection effects for instance, should most probably lead to a similar agreement with the experiments as reported in this paper but for a different value of supersaturation. The supersaturation 2 seems indeed a bit too high compared to experiments in capillary tubes ($\sigma \approx 1.6$–1.7) for example. Thus the conclusion on supersaturation should be regarded as more qualitative than quantitative. The crucial conclusion is that the consideration of a significant supersaturation effect is necessary to obtain a good agreement with our experiments.

As mentioned before, the existence of a significant supersaturation for sodium-chloride crystallization is however a controversial and in fact very important issue. According to current theory on damages induced by salt crystallization, the so-called crystallization pressure explicitly depends on the supersaturation level, e.g., Ref. 41. In brief, damages cannot be generated by crystallization without supersaturation. Interestingly, the experiments with limestone and sandstone samples reported in Ref. 42, led to the observation of serious damages, which cannot be explained in the absence of supersaturation. This suggests that supersaturation effects are not specific to the glass beads packings used in our experiments since supersaturation is also needed to explain the results reported in Ref. 42 for quite different porous media. However, the measurements using nuclear magnetic resonance (NMR) during drying of a fired-clay brick sample reported in Refs. 43–45, led to the opposite conclusion that no supersaturation was observed. Thus, we are left with at least two possibilities to explain the different conclusion reached in Refs. 43–45. The first one is that supersaturation is porous material dependent. Supersaturation would not exist in fired-clay brick because, for instance, of the existence of impurities allowing nucleation without noticeable supersaturation. The second possibility might be due to experimental limitations or to the consideration of average values for example. The results reported in Refs. 43–45 are in fact 1 mm thick slice averaged concentrations and not local values. According to our simulations the ion mass fraction is greater than the solubility mass fraction only in a narrow region adjacent to the surface of porous medium and even in fact in a small sub-region at the surface corresponding to the points of higher evaporation fluxes and preferential desaturation, at least for not too small Peclet numbers. This is illustrated in Fig. 11 for our situation. In the case of the results shown in Fig. 11, the supersaturation is 2 but the spatial average of the ion mass fraction at the surface $\langle c \rangle = \frac{1}{\pi r_c^2} \int_0^{r_c} 2\pi c(r) r\, dr = 0.19$, thus less than the solubility ($C_{sat} = 0.264$). Furthermore, it is quite likely that the supersaturation is in fact rapidly consumed once the crystals begin to grow (in a first phase when the growth is essentially controlled by the precipitation reaction). In other terms, it is expected that a quasi-equilibrium between the growing efflorescence and the solution is rapidly reached after this first phase. These two phases of the growth will be explained in more details in a forthcoming paper. Thus the consideration of slice averaged concentrations would not permit to identify a supersaturation effect in the case of the situation corresponding to Fig. 11. In other terms, the spatial and time resolution of the NMR experiments reported in the above-cited references might be insufficient to capture the supersaturation effect. This is of course a mere conjecture at this stage. We hope that the present discussion will stimulate further experiments so as to fully clarify this important issue.

X. CONCLUSIONS

We have studied numerically the impact of several factors affecting the distribution of ions in a drying porous medium and thus the first crystallization time at the surface of a porous medium. Four parameters play a fundamental role in the studied problem: the supersaturation σ, the parameter n (that is the retention curve, Fig. 6), the parameter α (that is the porosity wall effect Eq. (2)), the evaporation flux distribution Eq. (1). The method was to select or identify reasonable values for these parameters.

The study leads to the following conclusions:

(1) In a typical laboratory drying experiment, the evaporation flux is rarely uniform at the surface of the porous medium. This can have a great impact on the ion distribution and therefore on

the first crystallization time because the ion concentration increases faster in the region of high evaporation flux. In the case of our experiments this led to a nice porous medium coffee ring effect characterized by the formation of an efflorescence fairy ring at the surface of the porous medium.

(2) A second quite sensitive parameter is the porosity. The wall porosity effect leads to the preferential desaturation of the region of the porous medium near the wall, which in turn leads to local greater interstitial liquid velocities and thus a local increase in the ion mass fraction due to the enhanced advection effect. The local change in porosity near the wall has therefore a significant impact on the first crystallization time.

(3) Two main effects contribute to explain the dependence of first crystallization time with bead size. The first one is the gravity effect, which leads to non-uniform saturations along vertical lines with stronger variations as the bead size is increased. The second is related to the porosity wall effect, whose characteristic size decreases with a decreasing bead size. This variation is significant, about a decade in our experiments.

(4) The comparison between the experiments and the simulations indicates a significant supersaturation effect. This is an important conclusion in relation with the related problem of damages induced by the crystallization process since the so-called crystallization pressure explicitly depends on supersaturation, e.g., Ref. 41. This also poses a challenge to experimentalists since the properties of supersaturated aqueous solutions, notably the vapor pressure, needs to be characterized. Confirming the existence of supersaturation from direct *in situ* measurements in a drying porous medium would be also desirable.

(5) The findings reported in this paper can be generalized to other situations involving porous materials used in practice such as sandstone, limestone or brick. Similarly as in the situation studied in this paper, the location of first crystals at the surface will depend on the evaporation flux distribution along the evaporative surfaces and the capillary entry pressure spatial variations. It is hoped that the better understanding of the factors controlling the location of crystal will be instrumental in developing strategies for limiting the impact of salt weathering.

[1] A. Goudie and H. Viles, *Salt Weathering Hazards* (Wiley, Chichester, 1997).
[2] P. Lal, B. R. Chipa, and A. Kumar, *Salt Affected Soils and Crop Production: A Modern Synthesis* (Agrobios, Jodhpur, 2003).
[3] *Handbook of Industrial Drying*, 3rd ed., edited by A. S. Mujumdar (Taylor and Francis, Philadelphia, USA, 2007).
[4] Y. Peysson, B. Bazin, C. Magnier, E. Kohler, and S. Youssef, "Permeability alteration due to salt precipitation driven by drying in the context of CO_2 injection," Energy Procedia **4**, 4387 (2011).
[5] N. Sghaier and M. Prat, "Effect of efflorescence formation on drying kinetics of porous media," Transp. Porous Media **80**(3), 441 (2009).
[6] H. Eloukabi, N. Sghaier, M. Prat, and S. Ben Nassrallah, "Drying experiments in a hydrophobic model porous medium in the presence of a dissolved salt," Chem. Eng. Technol. **34**(7), 1085 (2011).
[7] H. Eloukabi, N. Sghaier, S. Ben Nasrallah, and M. Prat, "Experimental study of the effect of sodium chloride on drying of porous media: the crusty-patchy efflorescence transition," Int. J. Heat Mass Transfer **56**, 80 (2013).
[8] S. Veran-Tissoires, M. Marcoux, and M. Prat, "Discrete salt crystallization at the surface of a porous medium," Phys. Rev. Lett. **108**, 054502 (2012).
[9] S. Veran-Tissoires, M. Marcoux, and M. Prat, "Salt crystallization at the surface of a heterogeneous porous medium," Europhys. Lett. **98**, 34005 (2012).
[10] H. P. Huinink, L. Pel, and M. v. A. J. Michels, "How ions distribute in a drying porous medium: A simple model," Phys. Fluids **14**(4), 1389 (2002).
[11] L. Guglielmini, A. Gontcharov, A. J. Aldykiewicz, and H. A. Stone, "Drying of salt solutions in porous materials: Intermediate-time dynamics and efflorescence," Phys. Fluids **20**, 077101 (2008).
[12] N. Sghaier, M. Prat, and S. Ben Nasrallah, "On ions transport during drying in a porous medium," Transp. Porous Media **67**, 243 (2007).
[13] J. Van Brakel, "Mass transfer in convective drying," in *Advances in Drying*, edited by A. S. Mujumdar (Hemisphere, New York, 1980), pp. 217–267.
[14] R. D. Deegan, O. Bakajin, T. F. Dupont, G. Huber, S. R. Nagel, and T. A. Witten, "Capillary flow as the cause of ring stains from dried liquid drops," Nature (London) **389**, 827 (1997).
[15] S. Chatterji, "A discussion of the paper "Crystallisation in pores" by G. W. Scherer," Cem. Concr. Res. **30**, 669 (2000).
[16] G. W. Scherer, "Reply to the discussion by S. Chatterji of the paper, "Crystallization in pores"," Cem. Concr. Res. **30**, 673 (2000).
[17] J. Desarnaud and N. Shahidzadeh-Bonn, "Salt crystal purification by deliquescence - crystallization cycling," Europhys. Lett. **95**, 48002 (2011).
[18] H. Hu and R. G. Larson, "Evaporation of a sessile droplet on a substrate," J. Phys. Chem. B **106**, 1334 (2002).

[19] S. Beyaghi, S. Geoffroy, M. Prat, and K. M. Pillai, "Wicking and evaporation of liquids in porous wicks: A simple analytical approach to optimization," AIChE J. (to be published).
[20] S. Veran-Tissoires, S. Geoffroy, M. Marcoux, and M. Prat, "Evaporation and Wicking," in *Wicking in Porous Materials: Traditional and Modern Modeling Approaches*, edited by R. Masoodi and K. M. Pillai (CRC Press, Boca Raton, FL, 2012), Chap. 8.
[21] K. Vafai, "Convective flow and heat transfer in variable-porosity media," J. Fluid Mech. **147**, 233 (1984).
[22] J. Bear and A. Verruijt, *Modeling Groundwater Flow and Pollution* (Reidel, Dordrecht, 1987).
[23] R. A. Robinson, "The vapour pressures of solutions of potassium chloride and sodium chloride," Trans. R. Soc. N. Z. **75**(2), 203 (1945).
[24] M. Kaviany, *Principles of Heat Transfer in Porous Media*, Mechanical Engineering Series (Springer-Verlag, New York, 1991).
[25] P. Moldrup, T. Olesen, T. Komatsu, P. Schjønning, and D. E. Rolston, "Tortuosity, diffusivity, and permeability in the soil liquid and gaseous phases," Soil Sci. Soc. Am. J. **65**, 613 (2001).
[26] M. T. van Genuchten, "A closed-form equation for predicting the hydraulic conductivity of unsaturated soils," Soil Sci. Soc. Am. J. **44**, 892 (1980).
[27] F. A. L. Dullien, C. Zarcone, I. F. Macdonald, A. Collins, and R. D. E. Bochard, "The effects of surface roughness on the capillary pressure curves and the heights of capillary rise in glass bead packs," J. Colloid Interface Sci. **127**(2), 362 (1989).
[28] J. A. Dodds and P. Srivastava, "Capillary pressure curves of sphere packings: correlation of experimental results and comparison with predictions from a network model of pore space," Part. Part. Syst. Charact. **23**, 29 (2006).
[29] P. Lehmann and D. Or, "Evaporation and capillary coupling across vertical textural contrasts in porous media," Phys. Rev. E **80**(4), 046318 (2009).
[30] M. Prat, "Recent advances in pore-scale models for drying of porous media," Chem. Eng. J. **86**(1–2), 153 (2002).
[31] W. Masmoudi and M. Prat, "Heat and mass transfer between a porous medium and a parallel external flow, application to drying of capillary porous materials," Int. J. Heat Mass Transfer **34**(8), 1975 (1991).
[32] T. Defraeye, B. Blocken, D. Derome, N. Bart, and J. Carmeliet, "Convective heat and mass transfer modelling at air-porous material interfaces: overview of existing methods and relevance," Chem. Eng. Sci. **74**, 49 (2012).
[33] P. L. Kelly-Zion, C. J. Pursell, S. Vaidya, and J. Batra, "Evaporation of sessile drops under combined diffusion and natural convection," Colloids Surf., A **381**(1–3), 31 (2011).
[34] M. Prat, "Pore network models of drying, contact angle and films flows," Chem. Eng. Technol. **34**(7), 1029 (2011).
[35] F. A. San Martin, J. B. Laurindo, and L. A. Segura, "Pore-scale simulation of drying of a porous media saturated with a sucrose solution," Drying Technol. **29**, 873 (2011).
[36] A. G. Yiotis, A. G. Boudouvis, A. K. Stubos, I. N. Tsimpanogiannis, and Y. C. Yortsos, "The effect of liquid films on the drying of porous media," AiChE J. **50**(11), 2721 (2004).
[37] M. Prat, "On the influence of pore shape, contact angle and film flows on drying of capillary porous media," Int. J. Heat Mass Transfer **50**, 1455 (2007).
[38] F. Chauvet, P. Duru, S. Geoffroy, and M. Prat, "Three periods of drying of a single square capillary tube," Phys. Rev. Lett. **103**, 124502 (2009).
[39] F. Chauvet, P. Duru, and M. Prat, "Depinning of evaporating liquid films in square capillary tubes: influence of corners roundness," Phys. Fluids **22**, 112113 (2010).
[40] B. Camassel, N. Sghaier, M. Prat, and S. Ben Nasrallah, "Ions transport during evaporation in capillary tubes of polygonal cross section," Chem. Eng. Sci. **60**, 815 (2005).
[41] G. W. Scherer, "Stress from crystallization of salt," Cem. Concr. Res. **34**, 1613 (2004).
[42] C. Noiriel, F. Renard, M. L. Doan, and J. P. Gratier, "Intense fracturing and fracture sealing induced by mineral growth in porous rocks," Chem. Geol. **269**, 197 (2010).
[43] L. Pel, H. P. Huinink, and K. Kopinga, "Ion transport and crystallization in inorganic building materials as studied by nuclear magnetic resonance," Appl. Phys. Lett. **81**(15), 2893 (2002).
[44] L. Pel, H. P. Huinink, and K. Kopinga, "Salt transport and crystallization in porous building materials," Magn. Reson. Imaging **21**(3–4), 317 (2003).
[45] L. Pel, H. P. Huinink, K. Kopinga, R. P. J. van Hees, and O. C. G. Adan, "Efflorescence pathway diagram: understanding salt weathering," Constr. Build. Mater. **18**(5), 309 (2004).
[46] N. Shahidzadeh, personal communication (2013).